

Recovery of the Lamé parameter μ in biological tissues

Lin Ji and Joyce McLaughlin

Department of Mathematics, Rensselaer Polytechnic Institute, Troy, NY 12180, USA

E-mail: jil@rpi.edu and mclauj@rpi.edu

Received 14 April 2003, in final form 22 August 2003

Published 4 November 2003

Online at stacks.iop.org/IP/20/1 (DOI: 10.1088/0266-5611/20/1/001)

Abstract

By cross-correlating successive ultrasonic scans of the biological tissue that is excited by a transient source on the surface, recent experiments show that elastic wave displacement during the interval between the two scans can be measured everywhere in the tissue. Assuming that we know the displacement history, $w(t, x)$, of a propagating shear wave everywhere, we identify the stiffness change inside the tissue in terms of the Lamé coefficient, μ . So, the goal is: find μ from w . In the experiment, we consider that there is a dominant frequency, τ , called a central frequency. We then take the Fourier transform of w (in time) and evaluate this transform at τ . Using this transform of the data, our method starts with the asymptotic expansion of geometrical optics. By tracing the amplitude change of the displacement along the geometrical rays as they travel into the medium, we are able to recover μ without directly taking derivatives of the displacement data.

1. Introduction

The elastic properties of abnormal tissue can be significantly different from those of normal tissue. This is seen very strongly by considering the speed of a propagating shear wave. In normal tissue, the shear wave speed is between 1 and 3 m s⁻¹, while in abnormal tissue, it can be more than double that amount. This paper is devoted to determining the shear wave speed as a function of the Lamé parameter μ from *interior* propagating shear wave displacement data. It is motivated by the so-called transient elastography technology developed by Fink etc [1, 16] and [17].

The paper is structured as follows. In the rest of this introduction section, we first give a brief overview of the elastography technology and its associated ultrasound technique that makes it possible to measure *interior* displacement. We then establish the mathematical model that can be used to describe the propagating shear wave in transient elastography experiments. Section 2 is devoted to the mathematical analysis of geometrical optics theory that gives the foundation for the derivation of a differential algebraic system presented in section 3. This ODE algebraic system in which the measured displacement data are embedded is the core

of the inverse algorithm that we develop and formulate in section 4. It is the solution to this ODE algebraic system that gives us the Lamé parameter μ that we recover. Numerical experiments are demonstrated in section 5 and some discussion of the regularization that is used in the algorithm is given in section 6. In the conclusion of section 7, we summarize our achievements and the limitation of the method.

Depending on the way in which a boundary force is applied, elastography experiments can be divided into three categories:

- **Static experiments:** the tissue is deformed by a static or a slowly varying boundary force on a timescale that is slow enough that no elastic waves can be observed. In this case, the elasticity change is indicated by an image of the static displacement field where small displacement identifies hard (abnormal) tissue, see [14] and [15].
- **Dynamic excitation:** a time harmonic wave is created inside the tissue by a time harmonic boundary excitation. By carefully choosing the frequencies of boundary excitation, Parker and others (in [5, 19] and [25]) show images that are made from the standing wave pattern of the displacement field where again small magnitude of displacement identifies hard (abnormal) inclusions.
- **Transient elastography:** a short pulsed excitation is applied on the boundary so that a propagating shear wave is created inside the tissue. The time varying displacement is measured either by means of ultrasound or MRI and the goal is to recover the shear stiffness Lamé parameter μ as it varies throughout the region. Large μ identifies stiff inclusions.

As mentioned in the beginning of this section, the inverse algorithm presented in this paper is based on transient elastography. Figure 1 is a schematic diagram that shows the setup of a typical transient elastography experiment used in Fink's laboratory [16] where an electromagnetically controlled two-bar vibrator is used to produce the boundary traction force. The induced shear wave in the centre plane between the two bars is then captured by an ultrafast ($5000 \text{ images s}^{-1}$) ultrasound pulse–echo system that consists of a 128-element array of ultrasound transducers. The array is placed above the centre imaging plane and is parallel to the two bars. The transducers are responsible for both sending out pulses and recording the echoes which are analysed by the cross-correlation technique in order to get the time and space dependent displacement on a grid throughout the imaging plane. At each grid point, the displacement is then determined on a timescale of 0.2 ms with the ultrafast ($5000 \text{ images s}^{-1}$) ultrasound pulse–echo system.

Traditionally, the Doppler technique has been a very popular method for analysing the echo signal and determining the velocity of motion within the body, particularly in the measurement of blood flow. When it comes to assessing the local motion of soft tissue, however, the time-domain cross-correlation technique of ultrasonic imaging is becoming more and more widespread due to some potential advantages over the frequency-domain Doppler technique. It measures the displacement between two signals by locating the peaks of their cross-correlation function. Walker and Trahey (in [24]) show that this technique can measure displacements along the ultrasonic beam of the order of μm for a tissue slice of typically 1 mm. A good review of the time-domain cross-correlation technique can be found in [7]. In this paper, we shall assume that the local displacement as a function of time has been determined to the accuracy that can be achieved by time correlation techniques, has been interpolated between the grid points where the correlation technique has been applied and so is then known everywhere in the tissue. It is our task to identify the elasticity or the mechanical stiffness of the tissue from the data on the displacement field.

In the case of small deformation where linear elasticity dominates and the viscosity can be ignored, the dynamic response of an isotropic medium to the strike of an external force at the boundary, Γ , is modelled by the elastic wave equation

$$\nabla(\lambda \nabla \cdot \vec{w}) + \nabla \cdot \mu(\nabla \vec{w} + \nabla \vec{w}^T) - \rho \vec{w}_{tt} = 0 \quad (1.1)$$

with the boundary condition

$$\sigma \vec{n} = \vec{g}(t, x), \quad x \in \Gamma. \quad (1.2)$$

Here in equation (1.1), $\vec{w}(t, x)$ denotes the local displacement vector, ρ is the density of the medium, λ and μ are the Lamé coefficients describing the elasticity of the medium. The stress tensor, σ in (1.2), is given by

$$\sigma = \lambda \nabla \cdot \vec{w} I + \mu(\nabla \vec{w} + (\nabla \vec{w})^T)$$

and \vec{n} is the outward normal to Γ . The two principle wave types associated with the elastic material are the compressional wave travelling at the speed of $\sqrt{(\lambda + 2\mu)/\rho}$ and the shear wave travelling at the speed of $\sqrt{\mu/\rho}$. For typical soft tissue, λ is far greater than μ , while in normal tissue, $\sqrt{\mu/\rho}$ is small, typically from 1 to 3 m s⁻¹, and $\sqrt{(\lambda + 2\mu)/\rho}$ is nearly 1500 m s⁻¹. Furthermore, the variation in $(\lambda + 2\mu)/\rho$ is at most about 5%, while μ/ρ in abnormal tissue may be more than double its value in normal tissue. We are therefore mainly interested in recovering μ/ρ or the shear wave speed from the measured shear wave displacements.

Furthermore, since the compressional wave travels very fast through the imaging plane and is followed by the much slower shear wave, this makes it possible to distinguish between the two waves. For this reason, in this paper we use an approximate model for the downward component; that is, like Sandrin and Fink [16], we assume that we only need to consider the 2D scalar wave equation to model the downward component of the shear wave displacement in the imaging area for the two-bar device; see figure 1. The inverse algorithm developed here is extended to the full elastic wave equation in a separate paper [10]. The 2D scalar wave equation has the form

$$\nabla \cdot (c_0^2 \mu \nabla w) - \rho w_{tt} = 0, \quad (1.3)$$

where we keep the notation w and normalize the original $\sqrt{\mu/\rho}$ in (1.1) by a constant c_0 referred to as the background shear wave speed. Further, the density ρ will be assumed to be constant, $\rho \equiv 1$. The function μ after normalization describes the relative change of stiffness in the medium. We shall call it the stiffness profile of the medium and require that μ has twice-continuous derivatives.

Without losing generality, we regard the target tissue as a half-space domain ($x_1 \geq 0$). Placing the external force on the boundary, $x_1 = 0$, we then consider the following simplified model:

$$\nabla \cdot (c_0^2 \mu \nabla w) - w_{tt} = 0, \quad x_1 > 0, \quad (1.4)$$

and the boundary source

$$\frac{\partial w}{\partial x_1} = g(t) \quad \text{at } x_1 = 0, \quad (1.5)$$

where we also assume $\mu \equiv 1$ on the boundary $x_1 = 0$. The source function $g(t)$ is independent of x' representing a plane wave source. Although we are actually computing with a 2D scalar wave equation in this paper, we shall proceed with the general n -dimensional wave equation whenever possible and we expect that the same technique can be extended to the full model of the elastic wave equation without fundamental change of the essential idea. Throughout the paper, we use the notation x_1 for the depth variable with the positive direction pointing downward and x' for the horizontal space variable.

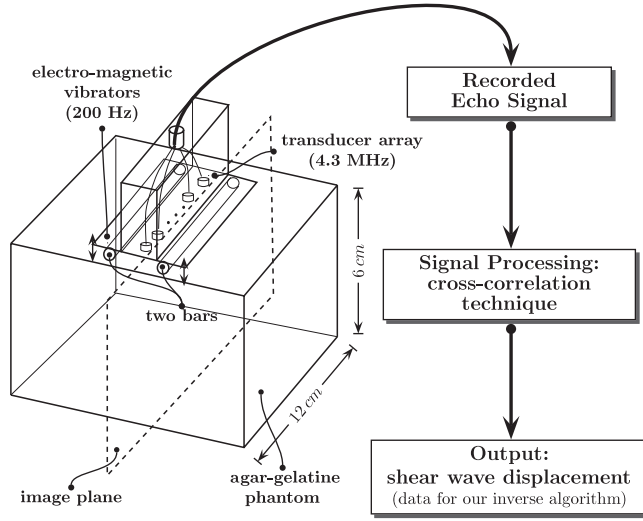


Figure 1. The device that is used by Sandrin and Fink etc [16] to excite the target tissue and to measure the shear wave motion at the same time.

2. The asymptotic expansion of geometrical optics

Our inverse algorithm is based on an algebraic equation that relates μ approximately to the amplitude of the shear wave displacement at each interior point. It is an approximate relation because we use the asymptotic expansion of geometrical optics to represent the displacement field. In this section, we develop the geometrical optics theory that is needed to derive this algebraic equation. An informal analysis of the accuracy of using the geometrical optics approximation is given in appendix C.

In experiments, e.g. in those done by Catheline *et al* [1, 16], the source on the boundary carries a central frequency. It is the central frequency content of the displacement data that we use as the direct input for our inverse algorithm. Taking the Fourier transform of (1.4) in time, we obtain the Helmholtz equation

$$\nabla \cdot (\mu \nabla u) + \kappa^2 u = 0, \quad x_1 > 0, \quad (2.1)$$

and the boundary condition

$$\frac{\partial u}{\partial x_1} \Big|_{x_1=0} = f(\tau), \quad (2.2)$$

$$\lim_{r \rightarrow \infty} \left(\frac{\partial u_s}{\partial r} - i\kappa u_s \right) / \sqrt{r} = 0, \quad u_s = u - \hat{g}(\tau) e^{i\kappa x_1} / i\kappa, \quad (2.3)$$

where $r = |x|$, $\kappa = \tau/c_0$ and

$$u(\tau, x) = \frac{1}{2\pi} \int w(t, x) e^{-it\tau} dt,$$

$$f(\tau) = \frac{1}{2\pi} \int g(t) e^{-it\tau} dt,$$

are the Fourier transforms of w and g in time. Equation (2.3) represents the outgoing Sommerfeld radiation condition. We expect the largest contribution of the Fourier transform to be at the central frequency and so fix τ at that value.

According to the theory of geometrical optics [11, 13], we make the following ansatz:

$$u(\tau, x) = a(\kappa, x)e^{i\kappa\phi(x)} \quad (2.4)$$

for the solution of (2.1) where the amplitude, $a(\kappa, x)$, is expanded into the form

$$a \sim a_0(x) + \frac{a_1(x)}{i\kappa} + \frac{a_2(x)}{(i\kappa)^2} + \dots \quad (2.5)$$

which is asymptotic as $\kappa \rightarrow +\infty$. Plugging (2.4) into equation (2.1) and setting the coefficient of each power of $i\kappa$ equal to zero, we get from the coefficient of the highest power of $i\kappa$ the eikonal equation for the phase:

$$|\nabla\phi|^2 - \frac{1}{\mu} = 0 \quad (2.6)$$

and from the coefficients of the remaining powers of $i\kappa$ the transport equations for the amplitude:

$$2\mu\nabla a_0 \cdot \nabla\phi + \mu a_0 \Delta_x \phi + a_0 \nabla\mu \cdot \nabla\phi = 0, \quad (2.7)$$

$$2\mu\nabla a_m \cdot \nabla\phi + \mu a_m \Delta_x \phi + a_m \nabla\mu \cdot \nabla\phi = -\mu \Delta_x a_{m-1} - \nabla\mu \cdot \nabla a_{m-1}, \quad m = 1, 2, \dots \quad (2.8)$$

A sufficient condition for solutions of these equations to yield an asymptotic series (2.5) in any compact set K in \mathbb{R}^n is that for any $\alpha = (\alpha_1, \alpha_2, \dots, \alpha_n)$, $0 \leq |\alpha| \leq 2$ [13],

$$\sup_{x \in K} \left| \frac{\partial^\alpha \phi}{\partial x^\alpha} \right| \leq C_K \quad \text{and} \quad \sup_{x \in K} \left| \frac{\partial^\alpha a_m}{\partial x^\alpha} \right| \leq C_K \sup_{x \in K} |a_m|, \quad m = 1, 2, \dots, \quad (2.9)$$

with C_K a constant that depends on K but is independent of κ . We note that C_K has to be of the order of $(i\kappa)^0$. In fact, it has to be significantly smaller than κ if we want to approximate the solution of (2.1) by the first one or two terms in the asymptotic expansion (2.5). To make it easy to see how big κ and further how big the central frequency, τ , of the source should be, we choose the length unit such that the size of the stiffness is roughly of unit length. In this way, the constant C_K can be kept $O(1)$. We shall come back to the issue of length scale later in this paper.

Our goal is to solve the inverse problem: find μ from u . However, prior to explaining our algorithm for doing this, we explain how (2.6), (2.7) and (2.8) are solved if μ is known. From here on, we will assume that μ is twice continuously differentiable and that there exist $\epsilon_1, \epsilon_2 > 0$ with $0 < \epsilon_1 < \mu$, $0 < \epsilon_2 < 1/\mu$. Returning to the problem at hand, we use the method of characteristics. The associated characteristic ODE for solving the first-order partial differential equation (2.6) when μ is known is given by [3]

$$\frac{dx}{ds} = 2p, \quad (2.10)$$

$$\frac{dp}{ds} = \nabla \frac{1}{\mu}, \quad (2.11)$$

$$\frac{d\phi}{ds} = \frac{2}{\mu}, \quad (2.12)$$

where p denotes $\nabla\phi$. Following the characteristic curves or rays $x(\cdot)$, the transport equations (2.7) and (2.8) become

$$\frac{da_0}{ds} = -a_0 \left(\Delta\phi + \frac{1}{\mu} \nabla\mu \cdot \nabla\phi \right), \quad (2.13)$$

$$\frac{da_n}{ds} = -a_n \left(\Delta\phi + \frac{1}{\mu} \nabla\mu \cdot \nabla\phi \right) - \Delta a_{n-1} - \frac{1}{\mu} \nabla\mu \cdot \nabla a_{n-1}, \quad n = 1, 2, \dots \quad (2.14)$$

From (2.13) and (2.14) together with (2.11) and (2.12), one can see that the amplitude a changes as μ changes along the ray. Therefore, it is our goal to solve the inverse problem: recover μ by using the amplitude change of the solution (2.4) along the rays as they travel into the unknown medium. The direction of the ray varies as the ray parameter, s , changes. Ideally, we want the ray to penetrate deeper and deeper into the medium as s increases so that we can recover the value of μ for every increase in depth. There are also difficulties with the ansatz for the expansion (2.5) if the ray direction is parallel to the medium boundary. This is the so-called grazing ray case. To avoid the discussion of grazing rays which requires more advanced microlocal techniques [20–22], for now we shall only consider rays along which the following non-grazing condition:

$$p_1 = \phi_{x_1} > \epsilon_0 \quad (2.15)$$

is met for some fixed $\epsilon_0 > 0$.

By choosing the boundary source appropriately at $x_1 = 0$ as we shall see later, we can have the condition (2.15) satisfied for all the rays $x(s)$ at $s = 0$ ($x_1(0) = 0$). As they travel into the medium, some of the rays may become grazing if there is a high contrast of stiffness in the region. Such rays will be ignored when they violate the non-grazing condition. Since

$$\frac{dx_1}{ds} = 2p_1,$$

the non-grazing condition (2.15) clearly means that these rays must go downward. This also enables us to make one helpful technical change. We can change the evolving variable from s to x_1 . Using x_1 , then, as the independent variable, the characteristic ODE for the eikonal equation becomes given by

$$\frac{dx'}{dx_1} = \frac{p'}{p_1}, \quad (2.16)$$

$$\frac{dp'}{dx_1} = \frac{1}{2p_1} \nabla_{x'} \frac{1}{\mu}, \quad (2.17)$$

$$\frac{d\phi}{dx_1} = \frac{1}{\mu p_1}, \quad (2.18)$$

where $p' = \nabla_{x'} \phi$, $p_1 = \sqrt{1/\mu - |p'|^2}$ and the initial conditions for x' , p' and ϕ are assumed to be

$$y' = x'(0), \quad \xi' = p'(0) \quad \text{and} \quad \phi_0(y') = \phi(0, y').$$

For each $x_1 \geq 0$ such that (2.15) is satisfied, the solution $(x'(x_1; y', \xi'), p'(x_1; y', \xi'))$ to the ODE system (2.16) and (2.17) defines a map:

$$\begin{aligned} \Pi_{x_1} : \mathbb{R}^{n-1} \times \mathbb{R}^{n-1} &\longmapsto \mathbb{R}^{n-1} \times \mathbb{R}^{n-1}, \\ (y', \xi') &\longmapsto \Pi_{x_1}(y', \xi') = (x'(x_1; y', \xi'), p'(x_1; y', \xi')). \end{aligned} \quad (2.19)$$

We now want to replace equation (2.13) by an identity relating the amplitude explicitly to the value of μ . Our goal then in solving the inverse problem is to simultaneously solve (2.16), (2.17) and the new equation for x' , p' and μ with the amplitude assumed as given.

By the theory of Fourier integral operators [8] and [13], the map Π_{x_1} is a local diffeomorphism in the sense that the Jacobian $\nabla_{(y', \xi')} \Pi_{x_1}$ is nonsingular. For fixed ξ' , the map of Π_{x_1} projected onto the x' space:

$$\Lambda_{x_1} : y' \longmapsto x'(x_1; y', \xi'), \quad (2.20)$$

however, can be singular. In geometrical optics [12], the set of points $(x_1, x'(x_1; y', \xi'))$ where

$$J = \nabla_{y'} x'(x_1; y', \xi') \quad (2.21)$$

is singular is called the caustic. It forms an envelope of the rays. At a caustic, the amplitude a has a singularity ($|a| \rightarrow \infty$) and the asymptotic expansion of geometrical optics given by (2.4) and (2.5) is not valid. Away from the caustic, however, we have:

Theorem 2.1. *Along the characteristic curve $(x'(x_1; y', \xi'), p'(x_1; y', \xi'))$, the amplitude a_0 in the asymptotic expansion (2.5) satisfies*

$$\mu(x_1, x') a_0^2(x_1, x') p_1(x_1) = (\det J(x_1))^{-1} \mu(0, y') a_0^2(0, y') p_1(0) \quad (2.22)$$

where $\det J$ denotes the determinant of J .

The proof of the theorem is the typical ray tube argument in the literature of geometrical optics [4]. We provide the proof in appendix A for the convenience of the reader.

3. The differential algebraic system

Equation (2.22) can be used to find the algebraic equation in the differential algebraic system that we will use to solve the inverse problem. For later use, we solve (2.22) for μ and first discuss properties of this equation that we will take into account when we implement our algorithm.

Since $p_1 = \sqrt{1/\mu - |p'|^2}$, the rewriting of equation (2.22) produces a quadratic equation for $1/\mu(x_1, x')$:

$$\begin{aligned} (\mu(0, y') p_1(0))^2 |a_0(0, y')|^4 \left(\frac{1}{\mu}\right)^2 - |a_0(x_1, x')|^4 (\det J(x_1))^2 \left(\frac{1}{\mu}\right) \\ + |a_0(x_1, x')|^4 (\det J(x_1))^2 |p'(x_1)|^2 = 0. \end{aligned} \quad (3.1)$$

There are two solutions to (3.1):

$$\frac{1}{\mu}(x_1, x') = \frac{1}{2} \frac{|a_0(x_1, x')|^4}{|a_0(0, y')|^4} \left(\frac{\det J(x_1)}{\mu(0, y') p_1(0)} \right)^2 (1 \pm \sqrt{D}) \quad (3.2)$$

where

$$D = 1 - 4 \frac{|a_0(0, y')|^4}{|a_0(x_1, x')|^4} \left(\frac{\mu(0, y') p_1(0)}{\det J(x_1)} \right)^2 |p'(x_1)|^2. \quad (3.3)$$

The two solutions are distinguished from each other by the sign in front of \sqrt{D} . Since we assume that we know μ on the boundary, the choice of sign is clear at $x_1 = 0$ from looking at the sign of

$$\frac{1}{\mu}(0, x') - \frac{1}{2} \left(\frac{\det J(0)}{\mu(0, y') p_1(0)} \right)^2. \quad (3.4)$$

This can be simplified to looking at the sign of

$$1 - \frac{1}{2(1 - \mu(0, y') |\xi'|^2)} \quad (3.5)$$

if we notice that $\det J(0) = 1$ and $p_1^2 = 1/\mu - |p'|^2$ and that μ is positive. Along the ray, the right sign can be chosen according to the continuity of $1/\mu$ as long as D remains positive. The ambiguity arises when D becomes zero at some critical point along the ray. The following theorem helps clarify the situation when D becomes zero.

Theorem 3.1. *Along the ray, D becomes zero iff the angle between the ray and the x_1 axis is $\pm\pi/4$.*

Proof. From (2.22) and the definition of D in (3.3), we have

$$\begin{aligned} D &= 1 - 4(1 - \mu|p'|^2)\mu|p'|^2 \\ &= (1 - 2\mu|p'|^2)^2 \end{aligned} \quad (3.6)$$

which is a quadratic equation in terms of $\mu|p'|^2$. The minimum of D is then zero and this occurs iff $\mu|p'|^2 = 1/2$. Since $p_1^2 + |p'|^2 = 1/\mu$, we know that $D = 0$ iff

$$p_1 = |p'|,$$

i.e. the ray forms a $\pm\pi/4$ angle with the x_1 axis. \square

To find the correct sign at points beyond the critical point, say x_1^* where $D(x_1^*) = 0$, along the ray, we could examine the left-hand-side derivatives of \sqrt{D} of various orders, i.e. $d^n \sqrt{D}/dx_1^n$ ($n = 1, 2, \dots$) as $x \rightarrow x_1^-$. If the order of the first non-zero derivative is odd, we want to change the sign in front of \sqrt{D} in equation (3.2) as the ray passes through the critical point x_1^* . Otherwise, if the order of the first non-zero derivative is even, we keep the sign. Of course, arbitrarily high derivatives of \sqrt{D} may not exist since we only assume that μ is twice continuously differentiable. However, in practice, we have not had to go beyond $n = 2$.

Equation (3.2) provides an explicit formula for calculating $1/\mu$ provided that all the terms on the right-hand side of the equation are known. These include the bi-characteristics

$$\begin{aligned} x' &= x'(x_1; y', \xi'), \\ p' &= p'(x_1; y', \xi'), \end{aligned}$$

the determinant of J and the amplitude a_0 . In order to solve for x' , p' and $1/\mu$, we then need an equation for $\det J$ and a measurement of a_0 . We can find an ODE for $\det J$ and the determinant of J can be integrated along the rays. Before we derive the ODE for $\det J$, however, we first show how we estimate $|a_0|$ from the displacement data, $u(\tau, x)$, and discuss the accuracy of this estimation.

When κ is large enough that the leading term $a_0(x)$ is dominant in the asymptotic expansion (2.5), the initial ansatz (2.4) for the solution $u(\tau, x)$ allows us to approximate a_0 simply by

$$|a_0(x_1, x')| \approx |u(\tau, x)|. \quad (3.7)$$

The approximation, however, has the potential to produce complex $1/\mu$ while solving the quadratic equation (3.1) since, with an approximation for a_0 , D in equation (3.3) can become negative. This is most likely to happen when the ray approaches a caustic where we do not expect a good match between $|a_0|$ and $|u|$ (see appendix C). Since we compute along several rays simultaneously, we then eliminate rays when D becomes negative. Since the rays tend to get very close near a caustic, this elimination has the positive effect of keeping the rays being followed more evenly distributed. In the numerical experiment, we shall show such an example with relatively high stiffness contrast and how we get around it by the simple cut-off and interpolation technique.

Since the success of using equation (3.2) for the recovery of μ largely depends on the quality of the approximation (3.7), we give an informal error analysis by estimating the magnitude of the next term a_1 in the asymptotic expansion (2.5) in appendix C.

We return now to deriving the ODE for $\det J$. To do so, we follow the definition for J in (2.21). After differentiating the ODE (2.16) and (2.17) with respect to the initial value y' , we obtain

$$\frac{d}{dx_1} J = -\frac{1}{2p_1^3} p' \left(\nabla_{x'} \frac{1}{\mu} \right)^T J + \frac{1}{p_1} \left(I + \frac{p' p'^T}{p_1^2} \right) H, \quad (3.8)$$

$$\frac{d}{dx_1} H = \frac{1}{2p_1} \left[\nabla_{x'} \left(\nabla_{x'} \frac{1}{\mu} \right) - \frac{1}{2p_1^2} \nabla_{x'} \frac{1}{\mu} \left(\nabla_{x'} \frac{1}{\mu} \right)^T \right] J + \frac{1}{2p_1^3} \left(\nabla_{x'} \frac{1}{\mu} \right) p^T H, \quad (3.9)$$

where $H = \nabla_{y'} p'(x_1; y', \xi')$. We now have a closed differential algebraic system for x' , p' , J , H and $1/\mu$ made up of (2.16), (2.17), (3.2), (3.8) and (3.9) if we replace $|a_0|$ by the measured data $|u|$. We change the system slightly by replacing (3.8) by an equation for $\det J$ and (3.9) by an equation for

$$A = H J^{-1} = \nabla_{x'} (\nabla_{x'} \phi).$$

To obtain the equation for $\det J$, we note that once we know the equation (3.8) for the derivative of J , the derivative of $\det J$ can be calculated as

$$\begin{aligned} \frac{d}{dx_1} (\det J) &= \text{tr} \left(J^{-1} \frac{d}{dx_1} J \right) \det J \\ &= \left[-\frac{1}{2p_1^3} \left(\nabla_{x'} \frac{1}{\mu} \right) \cdot p' + \frac{\text{tr} A}{p_1} + \frac{p'^T A p'}{p_1^3} \right] \det J \end{aligned} \quad (3.10)$$

where $J(0) = I$ and hence $\det J(0) = 1$. From (3.8) and (3.9), it is not difficult to show that

$$\begin{aligned} \frac{dA}{dx_1} &= \frac{-1}{p_1} A^2 - \frac{A p' p'^T A}{p_1^3} + \frac{1}{2p_1^3} \left[\left(\nabla_{x'} \frac{1}{\mu} \right) p'^T A + A p' \left(\nabla_{x'} \frac{1}{\mu} \right)^T \right] \\ &\quad - \frac{1}{4p_1^3} \nabla_{x'} \frac{1}{\mu} \left(\nabla_{x'} \frac{1}{\mu} \right)^T + \frac{1}{2p_1} \frac{\partial^2}{\partial x'^2} \frac{1}{\mu}. \end{aligned} \quad (3.11)$$

We are all set then to solve the differential algebraic system (2.16), (2.17), (3.2), (3.10) and (3.11) once we determine the initial values

$$y' = x'(0), \quad \xi' = p'(0) = \nabla_{y'} \phi(0, y') \quad \text{and} \quad A(0) = \nabla_{y'} (\nabla_{y'} \phi(0, y')) \quad (3.12)$$

for the ODEs (2.16), (2.17) and (3.11). These initial values can be found from the boundary data as we write

$$u(\tau; 0, y') = a(0, y') e^{i\kappa \phi(0, y')} \quad (3.13)$$

where a is the amplitude of u and ϕ is the phase of u normalized by the big parameter, κ . From (3.13), $y' = x'(0)$ has to be chosen such that

$$|u(\tau, 0, y')| > \hat{\epsilon}_0 > 0 \quad \text{for some } \hat{\epsilon}_0.$$

Intuitively speaking, you do not expect to get the correct information about the phase or any information about the ratio of amplitude change if the initial amplitude is zero or below the noise level.

For the plane wave source, $u(\tau; 0, y')$ is constant across the horizontal space y' . Thus, the initial phase, $\phi(0, y')$, is also constant while the initial value, $y' = x'(0)$, can be any place on the boundary. From (3.12), we then have

$$p'(0) = 0 \quad \text{and} \quad A(0) = 0$$

which comply with the non-grazing condition (2.15). In fact, we have

$$\phi_{x_1} = \sqrt{\frac{1}{\mu(0, x')}} > 0 \quad \text{at } x_1 = 0 \quad (3.14)$$

and all the rays initially then go down into the medium perpendicular to the boundary. In this case, the condition (2.9) is also perfectly satisfied when we set

$$a_0 = |u(\tau; 0, y')| \quad \text{and} \quad a_n = 0, \quad n = 1, 2, \dots$$

Such a choice of initial values for the plane wave source helps to optimize the match between $|a_0|$ and $|u|$.

Finally, we need to determine $\mu(0, y')$. To do this, if the wave speed is constant across the boundary, we set

$$\mu(0, y') \equiv 1$$

by choosing the background wave speed, c_0 , to be the wave speed on the boundary. In this case, even if we do not know the wave speed on the boundary, we can still identify the relative stiffness distribution in the region.

On the other hand, if the boundary source, $f(\tau, x')$, is known in addition to the boundary displacement measurement, $u(\tau, 0, x')$, we have the following way to identify the value of $1/\mu$ on the boundary for any given background wave speed, c_0 . Plugging (2.4) into the boundary condition (2.2), we obtain

$$\left(a_{x_1} + i \frac{\tau}{c_0} \phi_{x_1} a \right) e^{ik\phi}|_{x_1=0} = f(\tau, y'). \quad (3.15)$$

Keeping only the leading term in both (2.4) and (3.15), we get

$$|u(\tau, 0, y')| \approx a_0(0, y') = \frac{c_0 |f(\tau, y')|}{|\tau \phi_{x_1}|}. \quad (3.16)$$

The replacement of ϕ_{x_1} by $\sqrt{1/\mu(0, y') - |\xi'|^2}$ in (3.16) thus gives us

$$\frac{1}{\mu}(0, y') = \left(\frac{c_0 |f(\tau, x')|}{\tau |u(\tau, 0, x')|} \right)^2 + |\xi'|^2$$

for any $y' \in \mathbb{R}^{n-1}$ s.t. $|u(\tau, 0, y')| \neq 0$ where τ , again, refers to the central frequency of the source.

Remark 3.2. It is also likely that in applications we might want to consider a point source on the boundary. In this case, for the 2D wave equation, the usual asymptotic expansion of geometrical optics does not provide a good approximation to $|a_0|$ by $|u|$ even when μ is constant. In [9], a new expansion using the Hankel function of the first kind is proposed for the 2D wave equation model with a point source.

4. The strategy for recovering μ

The discussion so far for calculating the characteristic and for computing $\det J$ and approximating a_0 along the characteristic generates the following ODE algebraic system:

$$\frac{dx'}{dx_1} = \frac{p'}{p_1}, \quad (4.1)$$

$$\frac{dp'}{dx_1} = \frac{1}{2p_1} \nabla_{x'} \frac{1}{\mu}, \quad (4.2)$$

$$\frac{d}{dx_1} (\det J) = \left[-\frac{1}{2p_1^3} \nabla_{x'} \frac{1}{\mu} \cdot p' + \frac{\text{tr } A}{p_1} + \frac{p'^T A p'}{p_1^3} \right] \det J, \quad (4.3)$$

$$\begin{aligned} \frac{dA}{dx_1} = & \frac{-1}{p_1} A^2 - \frac{A p' p'^T A}{p_1^3} + \frac{1}{2p_1^3} \left[\left(\nabla_{x'} \frac{1}{\mu} \right) p'^T A + A p' \left(\nabla_{x'} \frac{1}{\mu} \right)^T \right] \\ & - \frac{1}{4p_1^3} \left(\nabla_{x'} \frac{1}{\mu} \right) \left(\nabla_{x'} \frac{1}{\mu} \right)^T + \frac{1}{2p_1} \nabla_{x'} \left(\nabla_{x'} \frac{1}{\mu} \right), \end{aligned} \quad (4.4)$$

$$\frac{1}{\mu}(x_1, x') = \frac{1}{2} \frac{|a_0(x_1, x')|^4}{|a_0(0, y')|^4} \left(\frac{\det J(x_1)}{\mu(0, y') p_1(0)} \right)^2 (1 \pm \sqrt{D}) \quad (4.5)$$

$$\approx \frac{1}{2} \frac{|u(\tau, x_1, x')|^4}{|u(\tau, 0, y')|^4} \left(\frac{\det J(x_1)}{\mu(0, y') p_1(0)} \right)^2 (1 \pm \sqrt{\tilde{D}}) \quad (4.6)$$

and the initial conditions (plane wave source)

$$x'(0) = y', \quad p'(0) = 0, \quad \det J(0) = 1 \quad \text{and} \quad A(0) = \mathbf{0} \quad (4.7)$$

where D is defined in (3.3) and by substituting u for a_0 is approximated by

$$\tilde{D} = 1 - 4 \frac{|u(\tau, 0, y')|^4}{|u(\tau, x_1, x')|^4} \left(\frac{\mu(0, y') p_1(0)}{\det J(x_1)} \right)^2 |p'(x_1)|^2$$

in the inverse algorithm.

The unknowns in the ODE algebraic system are

$$\vec{v} := (x', p', \det J, A)^T \quad \text{and} \quad \mu \quad (\text{the target function}).$$

To give a clear view of the relations between the various unknowns in the system, we rewrite it in the abstract form

$$\frac{d\vec{v}}{dx_1} = \vec{h} \left(\vec{v}; \frac{1}{\mu}, \nabla_{x'} \frac{1}{\mu}, \nabla_{x'} \left(\nabla_{x'} \frac{1}{\mu} \right) \right), \quad (4.8)$$

$$\frac{1}{\mu}(x_1, x') = \eta(\vec{v}, u(\tau, x_1, x')), \quad (4.9)$$

showing explicitly that the right-hand side of (4.8) depends on the derivative of $1/\mu$ in the lateral direction. This feature makes it impossible to solve the differential algebraic system along a single ray. To overcome this difficulty, we parametrize $1/\mu$ and solve simultaneously along at least as many rays as we have unknown parameters.

To explain our technique, we start with the two-dimensional case so that the transverse variable space is one-dimensional. Our strategy is this: choose an open region Ω'_0 on the boundary $x_1 = 0$. Each point $y' \in \Omega'_0$ then initiates a ray into the unknown medium. The idea is to integrate along a number of these rays at the same time so that, at $x_1 > 0$, not only the values of $1/\mu$ but also its derivatives can be well approximated from (4.9) for each point in

$$\Omega'_{x_1} := \{x' \in \mathbb{R} \mid x' = \Lambda_{x_1}(y'), y' \in \Omega'_0\}$$

where Λ_{x_1} is the projected map defined in (2.20). Once μ , $\nabla_{x'} 1/\mu$ and $\nabla_{x'}(\nabla_{x'} 1/\mu)$ are computed, they can be plugged back into the ODE (4.8) to compute a good approximation to the right-hand-side function \vec{h} at x_1 . Conceptually, we will obtain a closed ODE system in this way.

To carry out our plan, we put μ in a finite dimensional space. In our case, a convenient choice for our parametrization is to use the space of piecewise smooth polynomials called B -splines. A brief review of the B -spline theory required in our algorithm is given in appendix B. At each depth x_1 , we write as a finite approximation to the target function, μ , in the horizontal space variable

$$\mu(x_1, \cdot) \approx \sum_{i=1}^N c_i B_i(x_1; \cdot) \quad (4.10)$$

where N is the dimension of the B -spline space. Given $\hat{N} \geq N$ sampling points, $\{x^{(i)}\}_{i=1}^{\hat{N}}$ at each depth x_1 , the coefficient $c = (c_1, c_2, \dots, c_N)^T$ is obtained by solving the following least squares problem:

$$\min_c \|Mc - \vec{b}\|^2. \quad (4.11)$$

That is, we obtain c by solving

$$M^T M c = M^T \vec{b}, \quad (4.12)$$

where $M = (m_{ij})_{\hat{N} \times N}$ and $\vec{b} = (b_1, b_2, \dots, b_{\hat{N}})^T$ are defined as

$$m_{ij} = B_j(x_1; x^{(i)}) \quad \text{and} \quad b_i = \mu(x_1, x^{(i)}). \quad (4.13)$$

Initially, a set of sampling points $S_0 = \{y^{(i)}\}_{i=1}^{\hat{N}}$, $\hat{N} \geq N$, is chosen on the boundary Ω'_0 of the region. Suppose, further, that $\vec{v}^{(i)}$, $1 \leq i \leq \hat{N}$, is the solution to the ODE (4.8) with initial condition

$$\vec{v}^{(i)}(0) = (y^{(i)}, 0, 1, 0)^T.$$

Then, the explicit formula (4.6) or (4.9) for $1/\mu$ is used to compute the vector \vec{b} in the linear system (4.12). Therefore,

$$b_i = 1/\eta(\vec{v}^{(i)}, u^{(i)}(x_1)) \quad (4.14)$$

where $u^{(i)}(x_1) = u(\tau, x_1, x'(x_1; y^{(i)}, 0))$. The set of sampling points needed for computing the vector coefficient, c , in (4.10) at depth $x_1 > 0$ is then

$$S_{x_1} = \{x^{(i)} = x'(x_1; y^{(i)}, 0)\}_{i=1}^{\hat{N}}.$$

From the definition for the matrix M in (4.13) and the calculation for \vec{b} in (4.14), we see that the coefficient, c , obtained by solving the least squares problem (4.11) is a smooth function of $\{\vec{v}^{(i)}\}_{i=1}^{\hat{N}}$ provided that $M^T M$ in (4.12) is nonsingular. This is guaranteed by the B -spline theory as long as the Schoenberg–Whitney condition (B.6) in theorem B.2 is satisfied in the transverse variable. Further, we will assume something stronger. To make sure that the components of c remain bounded, we require that in each transverse variable, the condition (B.6) is satisfied with the interval R_i replaced by

$$\hat{R}_i = (z^i + \delta, z^{i+k} - \delta) \quad (4.15)$$

where δ is some small number.

Let

$$V = (\vec{v}^{(1)}, \vec{v}^{(2)}, \dots, \vec{v}^{(\hat{N})}) \quad \text{and} \quad U = (u^{(1)}, u^{(2)}, \dots, u^{(\hat{N})}).$$

We rewrite (4.10) as

$$\mu(x_1, \cdot) = \sum_{i=1}^N c_i(V, U) B_i(x_1; \cdot) \quad (4.16)$$

to emphasize the dependence of c on the solution to the ODE (4.8) and the data u . With (4.16), the derivatives of $1/\mu$ are simply given by

$$\nabla_{x'} \frac{1}{\mu}(x_1, x') = -\frac{1}{\mu^2} \sum_{i=1}^n c_i(V, U) \nabla_{x'} B_i(x_1; x'), \quad (4.17)$$

$$\begin{aligned} \nabla_{x'} \left(\nabla_{x'} \frac{1}{\mu}(x_1, x') \right) &= \frac{2}{\mu^3} \left(\sum_{i=1}^n c_i(V, U) \nabla_{x'} B_i(x_1; x') \right)^2 \\ &\quad - \frac{1}{\mu^2} \sum_{i=1}^n c_i(V, U) \nabla_{x'} (\nabla_{x'} B_i(x_1; x')). \end{aligned} \quad (4.18)$$

Inserting (4.16)–(4.18) into (4.8), we get a closed ODE system of finite dimension for V :

$$\frac{dV}{dx_1} = F(x_1, V; U) \quad (4.19)$$

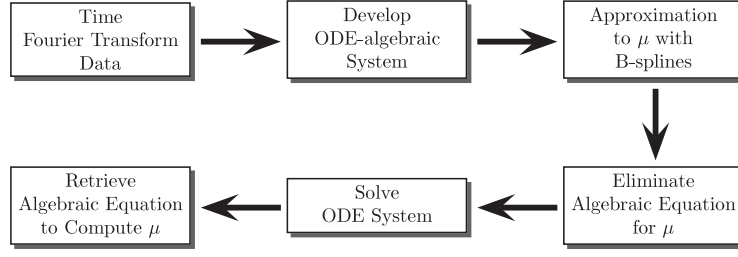


Figure 2. The flow chart of the analysis and the inverse algorithm.

where $F = (\vec{F}^{(1)}, \vec{F}^{(2)}, \dots, \vec{F}^{(\hat{N})})$ and

$$\vec{F}^{(i)}(x_1, V; U) = \vec{h}\left(\vec{v}^{(i)}; \frac{1}{\mu}, \nabla_{x'} \frac{1}{\mu}, \nabla_{x'} \left(\nabla_{x'} \frac{1}{\mu}\right)\right), \quad i = 1, 2, \dots, \hat{N},$$

and where μ , $\nabla_{x'} 1/\mu$ and $\nabla_{x'}(\nabla_{x'} 1/\mu)$ are given by (4.16)–(4.18). The initial condition for V is then

$$V(0) = ((y^{(1)}, 0, 1, 0)^T, (y^{(2)}, 0, 1, 0)^T, \dots, (y^{(\hat{N})}, 0, 1, 0)^T). \quad (4.20)$$

The inverse algorithm is simply solving the ODE system (4.19) with the initial condition (4.20). Once we have the solution V in the whole domain of interest, we obtain μ from (4.16). The main steps of the mathematical derivation and the inverse algorithm are summarized in figure 2.

It is important to address the questions of existence and uniqueness for the ODE system (4.19) and (4.20). Since we assume:

- (i) $|p_1| > \epsilon_0$;
- (ii) the sign for $\pm\sqrt{D}$ is chosen as long as $D \geq 0$ such that $\pm\sqrt{D}$ has a continuous derivative; $D > 0$ near the boundary $x_1 = 0$;
- (iii) $1/\epsilon_1 > 1/\mu > \epsilon_2 > 0$ for some fixed ϵ_1 and ϵ_2 ;
- (iv) the Schoenberg–Whitney condition (B.6) is satisfied with R_i replaced by \hat{R}_i in (4.15);

and the remaining dependence of F on V is explicit with bounded derivative $\nabla_V F$ as long as V is bounded; then $F(x_1, V)$ satisfies a Lipschitz condition. Then, the standard ODE theory tells us that:

Theorem 4.1. *Suppose we are given a connected set Ω_0 on the boundary of a half-space $\{x = (x_1, x') | x_1 > 0\}$. Let $y^{(1)}, \dots, y^{(\hat{N})}$ be (usually equally distributed) points in Ω_0 . Then, there exists a unique solution to (4.19), (4.20) in an interval $[0, x_1^M]$ with $x_1^M > 0$ where assumptions (i)–(iv) are satisfied.*

Proof. We only need to show that $\vec{v} = (x', p', \det J, A)^T$ is bounded. Since $|\mu|$ is bounded from assumption (iii) and a stronger Schoenberg–Whitney condition is imposed in assumption (iv), we know that the coefficients c_i , $i = 1, \dots, N$, in the B -spline representation (4.16) for μ are bounded. Therefore, the derivatives of $1/\mu$ in (4.17) and (4.18) are also bounded. Then, from assumption (i) and equations (4.1) and (4.2), the boundedness of x' and p' is obvious.

To obtain the boundedness of $\det J$ and A , we notice that the ordinary differential equations (4.3) and (4.4) for $\det J$ and $A = HJ^{-1}$ are derived from (3.8) and (3.9) which are linear ordinary differential equations in $J = \nabla_{y'} x'$ and $H = \nabla_{y'} p'$. By assumption (i) and our argument above about the boundedness of the derivatives of $1/\mu$, we then know that J and H are bounded and therefore $\det J$ is bounded. We also claim that $\det J > \epsilon_3 > 0$ for some

fixed ϵ_3 . Otherwise, $1/\mu \rightarrow 0$ as $\det J \rightarrow 0$ from equation (4.6). This violates assumption (iii). We finally obtain the boundedness for A from $A = HJ^{-1}$. \square

We make one more comment before we present the numerical results. As the characteristic rays approach a caustic they become closer together. This has three negative effects:

- (1) The first is that it creates the undesirable property of oversampling in that region.
- (2) The second is that near a caustic the solution $|u|$ is not well approximated by $|a_0|$ (see figure 8 (left)).
- (3) The third is the requirement that $D \geq 0$ can be violated when we replace $|a_0|$ by $|u|$.

This could have the undesired feature of stopping the algorithm just because one of our assumptions for theorem 4.1 is violated along one ray. For these reasons, we eliminate rays systematically when one of the assumptions (i)–(iii) is violated along those rays (see figure 8 (right)). As shown in the proof for theorem 4.1, such a strategy prevents the rays that we are using for our computation from approaching the caustic.

Note also that the opposite problem can occur. The rays may spread out and create under sampling with the result that assumption (iv), i.e. the Schoenberg–Whitney condition, is violated. In this case, we would add rays, a simple task at any value of \hat{x}_1 where we determine the initial values for the new rays by interpolation.

5. Numerical experiments

In our numerical experiments, we consider the wave equation in the 2D domain

$$\Omega := \{x \in \mathbb{R}^2 | 0 \text{ cm} \leq x_1 \leq 6 \text{ cm and } -6 \text{ cm} \leq x_2 \leq 6 \text{ cm}\}. \quad (5.1)$$

According to the typical shear wave speed in soft tissue, we choose

$$c_0 = 300 \text{ cm s}^{-1}$$

as the background wave speed. For the stiffness function μ , we use the Gaussian distribution

$$\mu = 1 + \delta\mu_{\max} \exp\left\{-\left(\frac{(x_1 - X_1^c)^2}{2\omega_1^2} + \frac{(x_2 - X_2^c)^2}{2\omega_2^2}\right)\right\} \quad (5.2)$$

centred at (X_1^c, X_2^c) . The size of the stiffness is roughly $2\omega_1 \times 2\omega_2$ (see figure 3).

Our choice of cm as the physical unit for length is not arbitrary here because of the argument we made about the length scale earlier in this paper. If we instead choose the metre (m) as the length unit, for a stiffness of size $0.01 \text{ m} \times 0.01 \text{ m}$, the constant C_K in the condition (2.9) could be on the order of 10^4 after taking the second derivative. This makes it difficult to determine how high we should choose the central frequency so that the lower order terms in the asymptotic expansion (2.5) can be neglected.

For the source function $g(t)$ in (1.5), we consider the plane wave source

$$g(t) = \frac{\cos(\tau(t - t_0))}{2\pi\epsilon_t} \exp\left\{-\frac{(t - t_0)^2}{2\epsilon_t^2}\right\} \quad (5.3)$$

which is independent of x_2 and has a Gaussian envelope in time (see figure 4 (left)). The source also carries a central frequency, τ .

In the extreme case where there is no stiffness change (i.e. $\delta\mu_{\max} = 0$ in (5.2)), the leading amplitude a_0 is constant for the plane wave source. The implication is that the constant C_K in (2.9) is zero. If we look at the transport equation (2.14) for the lower order terms, we see that they will be all zeros when a_0 is constant and $\Delta\phi = 0$ (which is true when $\mu \equiv 1$). In figure 4 (right), the plane wave source provides an exact match between $|u|$ and $|a_0|$ in the homogeneous medium.

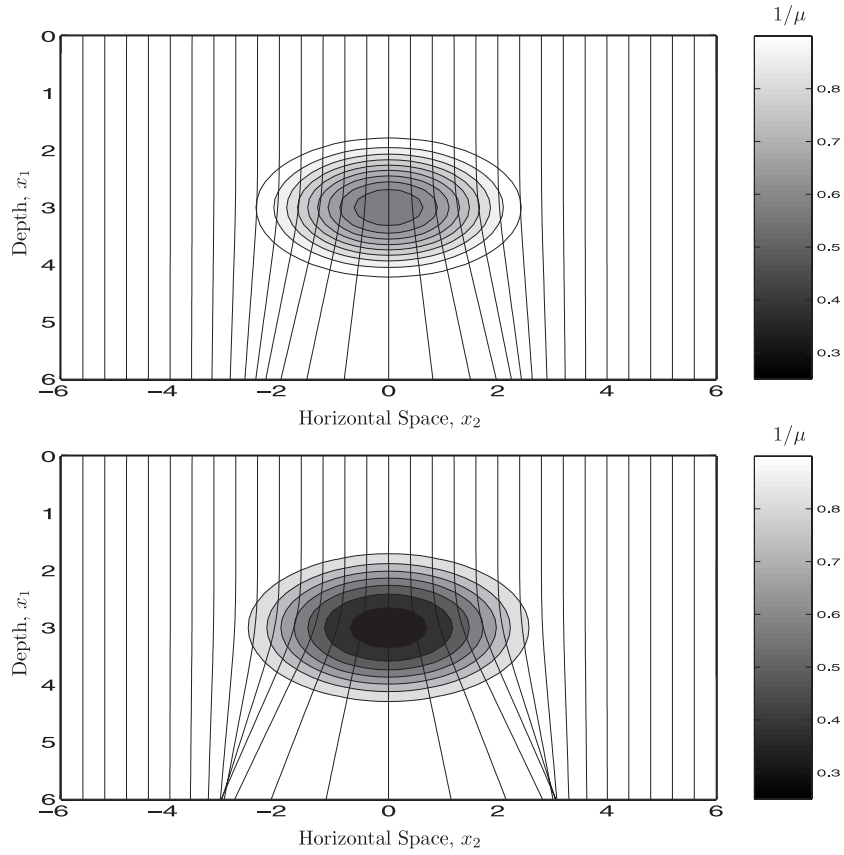


Figure 3. The contour of the stiffness function, $1/\mu$. The solid curves are geometrical optics rays coming down from the boundary at $x_1 = 0$. The stiffness in the top example is not strong enough to form caustics in the given region while the stiffness in the bottom example is strong enough to form caustics there.

With all these considerations in mind, for our first synthetic experiment we use the following parameters:

$$\delta\mu_{\max} = 1, \quad X_1^c = 3 \text{ cm}, \quad X_2^c = 0, \quad \omega_1 = 0.5 \text{ cm} \quad \text{and} \quad \omega_2 = 1 \text{ cm}$$

for μ . The stiffness in this example is not so strong. In fact, there is no caustic in the domain with such mild stiffness (see figure 3). For the central frequency, τ , of the source, we choose 200 Hz. With the background wave speed at 300 cm s^{-1} , 200 Hz is almost the lowest frequency needed for the inverse algorithm to succeed. The supposed big parameter κ in this case is only

$$\kappa = \frac{2\pi \times 200}{300} = 4.18.$$

The displacement data, $w(t, x)$, are simulated by numerically solving the wave equation adopting a finite element in space and finite difference in time scheme. In figure 5, we show the comparison between the exact $|a_0(x)|$ and its approximation $|u(\tau, x)|$. The exact a_0 is computed by solving the ODE system (4.1)–(4.4) with the exact $\mu(x)$ known. We then recover μ with the exact a_0 and $u(\tau, x)$ respectively. The results are shown in figure 6 side by side for comparison. Notice that there are some ripples below the stiffness bump in the case of using

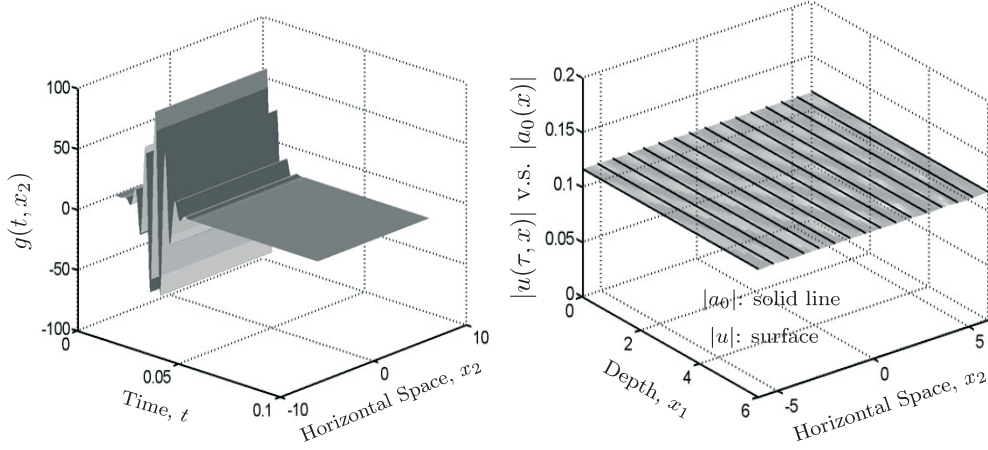


Figure 4. Left: the plane wave boundary source function, $g(t, x_2)$. Right: the approximation to $|a_0(x)|$ by $|u(\tau, x)|$ in the homogeneous medium for the plane wave source.

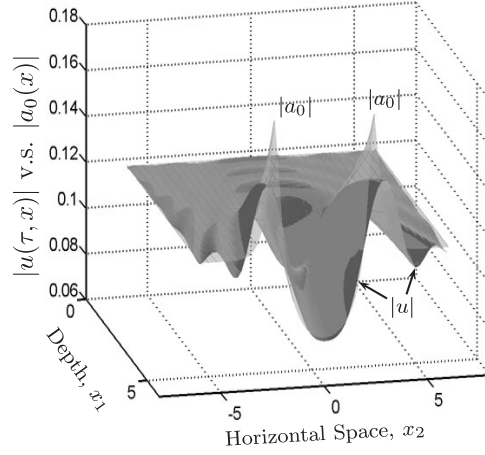


Figure 5. The comparison between the exact a_0 and $u(\tau, x)$ for the example depicted in the top of figure 3.

$u(\tau, x)$ for the recovery of μ . These are artifacts due to the large mismatch between a_0 and u after the wave passes through the stiffness region (see figure 5).

To test the stability of the inverse algorithm against noise, we add random noise to the shear wave displacement data, $w(t, x)$, in the following way:

$$\tilde{w}(t, x) = w(t, x) + \gamma w_{\max} r(t, x) \quad (5.4)$$

where $w_{\max} = \max_{t>0, x \in \Omega} |w(t, x)|$ (Ω is defined in (5.1)) is the maximum displacement, γ is the percentage of noise and $r(t, x)$ is a random number generated in Matlab from the normal distribution with mean zero, variance one and standard deviation one. After taking the Fourier transform of \tilde{w} in time to get $\tilde{u}(\tau, x)$, we recover μ from \tilde{u} . The result is shown in figure 7. Note that there is no preliminary filtering of either the original data, $\tilde{w}(t, x)$, or their Fourier transform, \tilde{u} , before we use them in our inverse algorithm. To minimize the influence of noise, we simply double the distance between the breaks for the construction of the B -splines so that

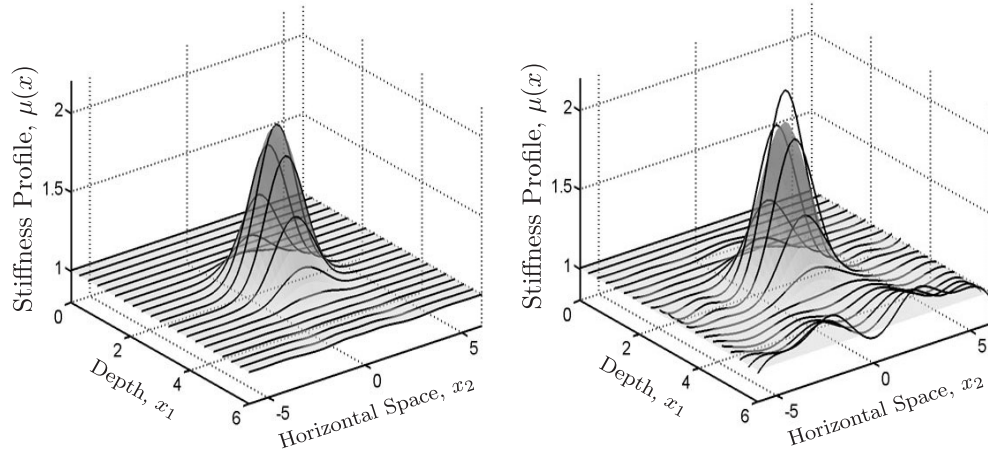


Figure 6. The μ recovered from the exact a_0 (left-hand figure) and from the data $u(\tau, x)$ (right-hand figure). The horizontal curves represent the recovered μ . The semi-transparent surface shows the true μ .

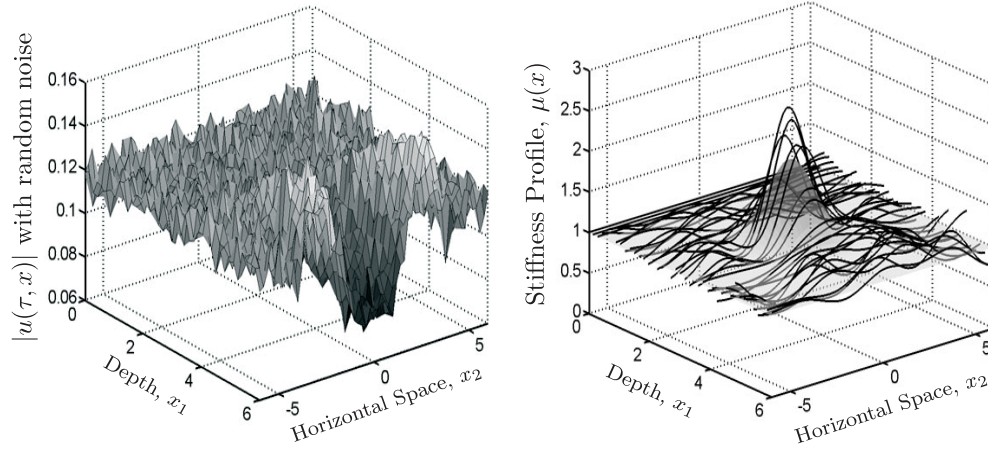


Figure 7. The μ recovered (horizontal curves in the right-hand figure) from the data $u(\tau, x)$ (left-hand figure) where 5% random noise is added according to (5.4). Note that the noise is added to the original data, $w(t, x)$, before they are Fourier transformed to $u(\tau, x)$. The semi-transparent surface in the right-hand figure shows the true μ .

there are about five data sampling points between the breaks. As we remarked in appendix B, solving the least squares problem (4.11) with more sampling points than the breaks has a smoothing effect.

For the second experiment, we increase $\delta\mu_{\max}$ from 1 to 3 so that caustics are formed right after the rays pass the region of stiffness (see figure 3). In this case, the exact amplitude a_0 grows to infinity at these caustics while the solution $u(\tau, x)$ to the Helmholtz equation (2.1) is finite (see figure 8). Therefore, the idea of using $u(\tau, x)$ to approximate a_0 gives a poor approximation around these points. In fact, the mismatch between $|u|$ and $|a_0|$, due to the strong contrast of the stiffness, becomes so big at $x_1 = 3.0$ that it fails to produce a real solution to the quadratic equation (3.1) for $1/\mu$ long before the caustics start to appear at $x_1 = 5$. As we

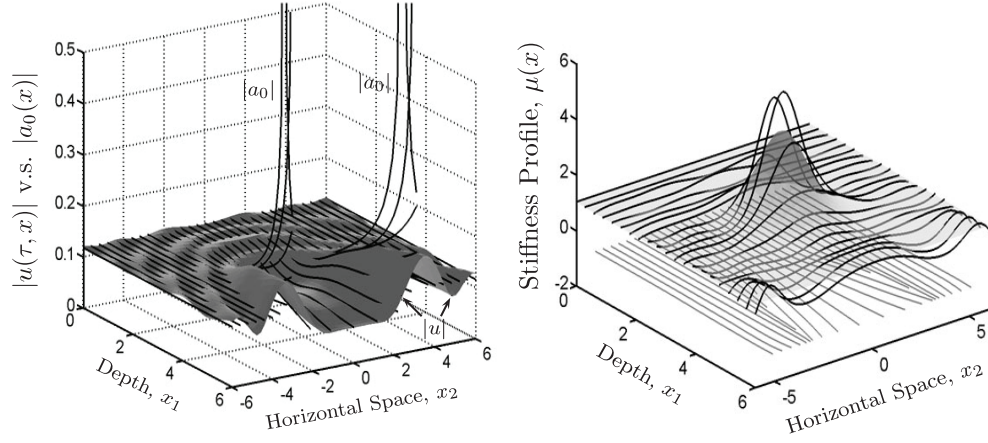


Figure 8. Left: in the case of strong stiffness, the amplitude, $|a_0|$, explodes to ∞ as the rays approach caustics. Right: the horizontal curves represent the recovered μ . The semi-transparent surface shows the true μ . The lines drawn in the depth direction at the bottom are the geometrical optics rays. The inverse algorithm ignores those rays when they fail to satisfy one of the assumptions (i)–(iii).

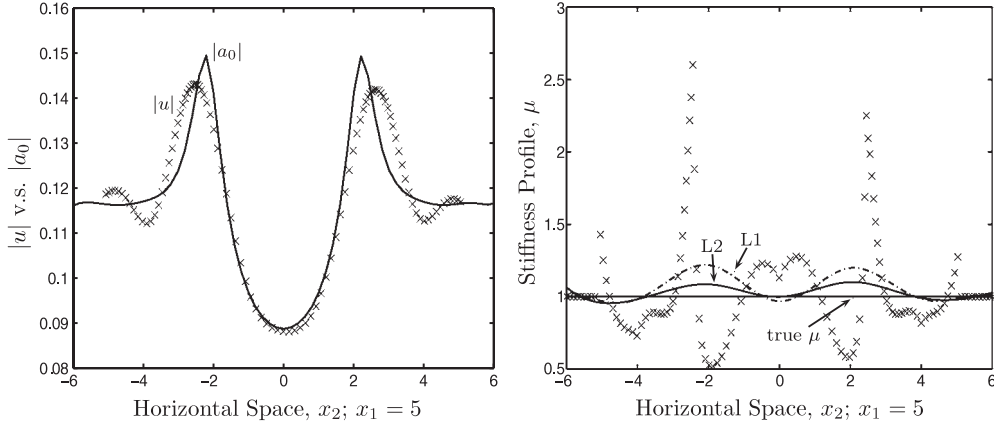


Figure 9. A snapshot of the recovery at $x_1 = 5$ from the first numerical example (figure 6). Left: the comparison between $|u|$ and $|a_0|$. Right: the crosses (\times) represent the μ calculated at each point using the data $|u|$ on the left. The dash-dot curve (L1) and the solid curve (L2) are the results from using B -spline interpolations of μ and $\mu^{1/4}$ respectively.

mentioned before, we get around the obstacle to the continuation of our algorithm by simply stopping those rays in our B -spline interpolation when they cannot give us real valued $1/\mu$. If figure 8 is examined closely, it can be seen that some of the rays are broken before they reach the bottom of medium. In this way, we also prevent the rays from going through the caustics.

6. About the regularization

The B -spline interpolation not only gives us a closed ODE system of finite dimension, it is also crucial for the regularization of the differential operation involved in the algorithm. Here, the density of the knot sequence required for the B -spline construction, i.e. the distance between

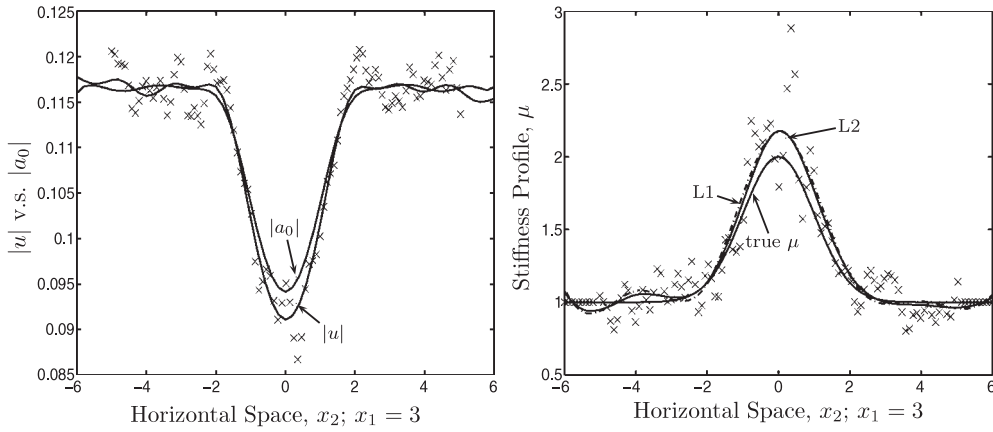


Figure 10. The cross section of figure 7 at $x_1 = 3$. Left: the crosses (\times) represent $|u|$ with noise. Right: the crosses (\times) represent the μ calculated using the noisy data shown on the left. The dash-dot curve (L1) and the solid curve (L2) are the results from using B -spline interpolations of μ and $\mu^{1/4}$ respectively. In this case, they are very close because there are no biased peak values of μ .

the knots, can be regarded as the regularization parameter. The distance has to be small enough in order to capture the sharp change in the stiffness but large enough in order to stabilize the differentiation and to smooth out random noise and some unwanted ripples due to scattering and the mismatch between $|a_0|$ and $|u|$. Figure 9 shows how such regularization works as the algorithm proceeds layer by layer. Notice how the calculated μ oscillates around the true μ because of the alternating difference between $|a_0|$ and $|u|$. They demonstrate the scattering effect of the inhomogeneity that is not captured by the asymptotic expansion of geometrical optics (2.4) after the wave passes the inhomogeneous region between $x_1 = 2$ and 4. The dash-dot curve shows the B -spline interpolation of μ with a knot sequence of 2 cm between the knots. Note how the oscillation is suppressed by the B -spline. In this example, we assume $\mu \equiv 1$ outside the boundary at $x_2 = \pm 6$.

Also notice in figure 9 that there are two peak values of μ around $x_2 = -2.5$ and 2.5. They are artifacts caused by the big difference between $|a_0|$ and $|u|$ when the rays approach the caustics. One possibility for reducing the bias of the two peaks is to replace the B -spline interpolation formula (4.16) by a similar formula to interpolate $\mu^{1/4}$ instead of μ and change the formulae (4.17), (4.18) for the derivatives accordingly. Let f_B denote the resulting B -spline. We then use $\mu_B = f_B^4$ as the final representation for μ . The result from our algorithm using this approximation is shown as the black solid curve (labelled L2) in figure 9 where we also show the result (dash-dot curve labelled L1) from directly interpolating μ for comparison.

To see the effect of random noise filtering by the B -spline, we show in figure 10 the intermediate interpolation used in the first numerical example with 5% added random noise (figure 7). The consequence of random noise is clearly manifested in the calculated μ (cross line) in figure 10 (right) and the smoothing effect of the B -spline is obvious.

7. Conclusion

In this paper, we develop an inverse algorithm that recovers the unknown Lamé parameter, μ , from the amplitude of the known *interior* displacement data, $|u(\tau, x)|$. Compared to an optimization approach [23] that requires repeatedly solving either the wave equation (1.4) or

the Helmholtz equation (2.1) at each updating step, our algorithm is fast because we only need to solve a system of ordinary differential equations simultaneously along a set of geometrical optics rays once. The current implementation of the algorithm in Matlab takes less than 5 min to run on a Sun Ultra 10 microsystem for the numerical examples shown in figure 3. Since the derivation of the ODE system is based on the theory of geometrical optics, the recovery is accurate to the approximation of a geometrical optics expansion.

By looking for μ in the B -spline space that is constructed from an appropriately chosen knot sequence, we introduce regularization through the least squares B -spline interpolation. In this way, our algorithm essentially avoids taking derivatives of the data explicitly except for the rare case when the sign in front of \sqrt{D} in (3.2) has to be resolved by looking at the derivatives of \sqrt{D} with D being defined in (3.3). Even in this case, what we differentiate is $|u(\tau, x)|$ ($|a_0| \approx |u|$) instead of $u(\tau, x)$ (or $w(t, x)$) which is more oscillatory than its absolute value, $|u(\tau, x)|$.

As we approach a caustic, some rays become very close together and the algorithm is made to be successful by systematically eliminating some of these rays. This also has the positive effect of eliminating oversampling of u which is a poor approximation of a_0 in this region.

We note also that when the stiffness change in μ increases to more than four times the background value, backscattering not represented in the geometrical optics expansion becomes significant. In this case, the recovery of μ with this algorithm becomes degraded. We have not, however, presented examples of this here.

Acknowledgments

We wish to thank Clifford Nolan for useful discussion regarding the theory of geometrical optics and microlocal analysis and his comments on the final draft of this paper. We also wish to thank Christophe Geuzaine, Jean-Francois Remacle and their software development team in Belgium for providing the PDE solver, GetDP [2], and the finite element meshing tool, Gmsh [6]. Their professionalism and quick responses to our questions regarding the use of the software were important to the success of this paper. We also acknowledge that Lin Ji's work is supported by NSF FRG Grant DMS-0101458 and J McLaughlin's work is partially supported by NSF Grant DMS-9983646 and NSF FRG Grant DMS-0101458, and partially supported by ONR Grant N00014-96-1-0349.

Appendix A. Proof of theorem 2.1

Theorem A.1. *Along the characteristic curve $(x'(x_1; y', \xi'), p'(x_1; y', \xi'))$, the amplitude a_0 in the asymptotic expansion (2.5) satisfies*

$$\mu(x_1, x') a_0^2(x_1, x') p_1(x_1) = (\det J(x_1))^{-1} \mu(0, y') a_0^2(0, y') p_1(0)$$

where $\det J$ denotes the determinant of J .

Proof. From the transport equation (2.7),

$$\nabla \cdot (\mu a_0^2 \nabla \phi) = 0. \tag{A.1}$$

Around each ray, we construct an infinitesimally thin tube, T , as depicted in figure A.1. such that the two ends of the tube, Γ_1 and Γ_3 , are parallel to the horizontal x' space while the side surface of the tube, Γ_2 , is parallel to the characteristic. Applying the divergence theorem in the tube, we have

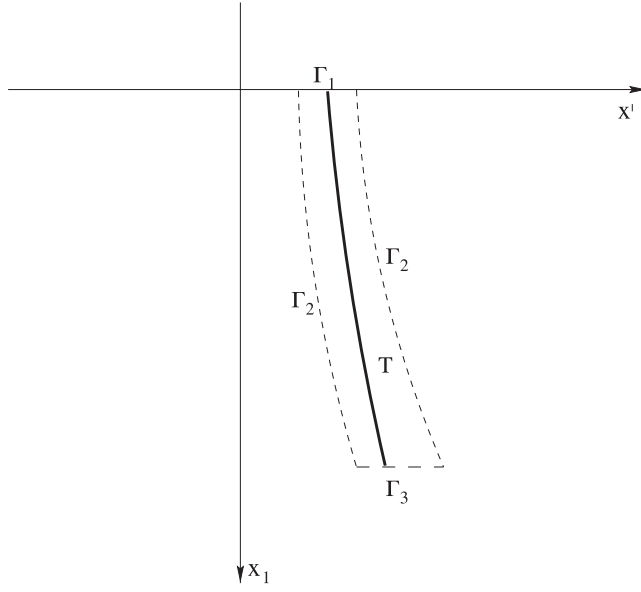


Figure A.1. The ray tube: constructed for the proof of theorem 2.1.

$$\begin{aligned} \int_T \nabla \cdot (\mu a_0^2 \nabla \phi) \, dv &= \int_{\Gamma_1 + \Gamma_2 + \Gamma_3} \mu a_0^2 \nabla \phi \cdot \vec{n} \, ds \\ &= I_1 + I_2 + I_3 \end{aligned}$$

where \vec{n} is the unit outward normal to the surface of the tube and

$$\begin{aligned} I_1 &= \int_{\Gamma_1} \mu a_0^2 \phi_{x_1} \, ds, \\ I_2 &= \int_{\Gamma_2} \mu a_0^2 \nabla \phi \cdot \vec{n} \, ds, \\ I_3 &= - \int_{\Gamma_3} \mu a_0^2 \phi_{x_1} \, ds. \end{aligned}$$

Since $\nabla \phi$ is tangential to the characteristic,

$$I_2 = 0.$$

By (A.1), we have

$$I_1 + I_3 = 0.$$

Since $\det J(x_1)$ represents the ratio between the cross sectional areas of the two ends, Γ_3 and Γ_1 , of the tube, we obtain (2.22) immediately. \square

Appendix B. The theory of B -spline approximation: a brief review

By selecting the right order and the appropriate sequence of knots, a B -spline can be used to approximate any smooth or even piecewise smooth function with arbitrary accuracy [18]. For B -splines on a 1D interval, this means that:

Theorem B.1. For any function $\zeta \in C^d[\alpha, \beta]$ and $\forall \epsilon > 0$, we can always select a fine enough knot sequence in $[\alpha, \beta]$:

$$s := (\alpha = z^1 \leq z^2 \leq \dots \leq z^\ell = \beta)$$

that the corresponding B -spline space of order $k \geq d + 2$ contains a spline:

$$\zeta_s = \sum_{i=1}^N c_i B_i \quad (\text{B.1})$$

that is close to ζ ; i.e.

$$\max_{z \in [\alpha, \beta]} \left| \frac{d^j}{dz} (\zeta_s - \zeta)(z) \right| \leq \epsilon, \quad 0 \leq j \leq d.$$

Here, $N = \ell - k$ is the dimension of the B -spline space and B_i is the i th B -spline with knots z^i, \dots, z^{i+k} . The $=$ sign in the sequence s indicates the possible multiplicity for each knot.

To construct a knot sequence, we first need to choose a strictly increasing sequence of breaks

$$\alpha = Z^1 < Z^2 < \dots < Z^L = \beta.$$

The knot sequence is simply a result of repeating each break with the appropriate multiplicity to control the smoothness at each break. A standard choice is to repeat the two end points α and β exactly k times but keep all the internal breaks Z^2, \dots, Z^{M-1} simple; in this case, the knot sequence is $\{z^1 = \dots = z^k = Z^1, z^{k+1} = Z^2, \dots, z^{k+L-2} = Z^{L-1}, z^{k+L-1} = \dots = z^{2k+L-2} = Z^L\}$. The resulting B -spline will have $k - 2$ continuity at each internal break and $k - 1$ continuity on each subinterval $[Z^j, Z^{j+1}]$.

Given the approximate form ζ_s for ζ then, and exactly N sampling points, $\{x^{(i)}\}_{i=1}^N$, in $[\alpha, \beta]$, the coefficient

$$c = (c_1, c_2, \dots, c_N)^T$$

in the approximation (B.1) can be obtained by solving the linear system

$$Mc = \vec{b} \quad (\text{B.2})$$

where $M = (m_{ij})_{N \times N}$ and $\vec{b} = (b_1, b_2, \dots, b_N)^T$ are defined as

$$m_{ij} = B_j(x^{(i)}) \quad \text{and} \quad b_i = \zeta(x^{(i)}). \quad (\text{B.3})$$

When there are $\hat{N} > N$ sampling points, which is what we choose in our implementation, the following least squares problem can be solved for c :

$$\min_c \|Mc - \vec{b}\|^2 \quad (\text{B.4})$$

where $M = (m_{ij})_{\hat{N} \times N}$ and, in this case, we obtain c by solving

$$M^T M c = M^T \vec{b}. \quad (\text{B.5})$$

The existence and uniqueness of the solution to both (B.2) and (B.5) is guaranteed by the following theorem [18]:

Theorem B.2. Let $\alpha \leq x^{(1)} < x^{(2)} < \dots < x^{(\hat{N})} \leq \beta$ be the sampling points. Then the matrix M defined by (4.13) or $M^T M$ in (4.12) is nonsingular if and only if the Schoenberg–Whitney condition is satisfied, i.e., there exists a subsequence $\alpha \leq x^{(j_1)} < x^{(j_2)} < \dots < x^{(j_N)} \leq \beta$ s.t.

$$x^{(j_i)} \in R_i := \begin{cases} [z^i, z^{i+k}) & \text{if } z^i = z^{i+k-1}, \\ (z^i, z^{i+k}) & \text{otherwise,} \end{cases} \quad (\text{B.6})$$

where R_i ($1 \leq i \leq N = \ell - k$) is the supporting interval for B_i .

Remark B.3. If the number of sampling points is much greater than the dimension of the B -spline space and they are evenly distributed, solving (4.11) can smooth out the effect of random noise or even round-off error in the sampled data as exhibited by our numerical experiments. This is especially important when we take the transverse derivatives of the target function.

Appendix C. The accuracy of the geometrical optics approximation

In this appendix, we give an informal analysis of the magnitude of the a_1 term in the asymptotic expansion (2.5). The purpose is to have an idea of the error in the approximation of u by the leading order term a_0 in (2.5).

Using x_1 as the evolving variable, the transport equation (2.14) for a_1 becomes

$$\frac{da_1}{dx_1} = -\frac{1}{2p_1} \left(\Delta\phi + \frac{1}{\mu} \nabla\mu \cdot \nabla\phi \right) a_1 - \frac{1}{2p_1} \left(\Delta a_0 + \frac{1}{\mu} \nabla\mu \cdot \nabla a_0 \right). \quad (\text{C.1})$$

If we assume $a_1(0) = 0$, the solution to (C.1) is given by

$$a_1 = e^{v(x_1)} \int_0^{x_1} \rho(s) e^{-v(s)} ds \quad (\text{C.2})$$

where

$$v(x_1) = \int_0^{x_1} -\frac{1}{2p_1} \left(\Delta\phi + \frac{1}{\mu} \nabla\mu \cdot \nabla\phi \right) dx_1,$$

$$\rho(x_1) = -\frac{1}{2p_1} \left(\Delta a_0 + \frac{1}{\mu} \nabla\mu \cdot \nabla a_0 \right).$$

The integral in (C.2) is integrated along the characteristic curve. Under the conditions of (2.9) and (2.15), we have

$$v \sim \mathcal{O}(1)x_1.$$

Thus,

$$|a_1| \leq e^{\mathcal{O}(1)x_1} \int_0^{x_1} |\rho(s)| ds.$$

Suppose that $\delta\mu$ and δa_0 represent the magnitudes of change in μ and a_0 respectively. We then have the following estimate for a_1 :

$$|a_1| \leq C_2 (1 + \delta\mu) \delta a_0 \frac{x_1 e^{\mathcal{O}(1)x_1}}{\delta x_1^2} \quad (\text{C.3})$$

where δx_1 is the length scale over which the changes in μ and a_0 develop. It is also reasonable to assume that δx_1 is the length scale of the stiffness region. As mentioned before, the length unit is chosen to be the length scale of the stiffness. Equation (C.3) then tells us that a_1 is of the same magnitude as the change in a_0 if the depth of the medium, x_1 , is not significantly bigger than δx_1 .

The above analysis shows that the approximation of u by a_0 can be accepted if the parameter $\kappa = \tau/c_0$ is reasonably big and assumption (2.9) is satisfied. This shows the limitation of using the geometrical optics approximation. To get an understanding of when (2.9) may not be satisfied, note that when there is a stiff region with relatively high contrast in the medium, caustics are likely to form. Depending on the magnitude of the stiffness, sooner or later the approximation along some rays will become invalid as they pass through the stiff region and approach the caustics. What happens is that the derivatives of the phase ϕ and of the geometrical optics amplitude a increase significantly around the caustics, so assumption (2.9) is no longer valid.

References

- [1] Catheline S, Thomas J-L, Wu F and Fink M 1999 Diffraction field of a low frequency vibrator in soft tissues using transient elastography *IEEE Trans. Ultrason. Ferroelectr. Freq. Control* **46** 1013–9
- [2] Dular P and Geuzaine C GetDP: a general environment for the treatment of discrete problems <http://www.geuz.org/getdp/>
- [3] Evans L C 1998 *Partial Differential Equations (GSM/19)* (Providence, RI: American Mathematical Society)
- [4] Friedlander F G 1958 *Sound Pulses* (Cambridge: Cambridge University Press)
- [5] Gao L, Parker K J and Alam S K 1995 Sonoelasticity imaging: theory and experimental verification *J. Acoust. Soc. Am.* **97** 3875–80
- [6] Geuzaine C and Remacle J-F Gmsh: a three-dimensional finite element mesh generator with built-in pre- and post-processing facilities <http://www.geuz.org/gmsh/>
- [7] Hein I A and O'Brien W D 1993 Current time-domain methods for assessing tissue motion by analysis from reflected ultrasound echoes—a review *IEEE Trans. Ultrason. Ferroelectr. Freq. Control* **40** 84–102
- [8] Hormander L 1971 Fourier integral operators I *Acta Math.* **127** 79–183
- [9] Ji L and McLaughlin J 2002 Using a Hankel function expansion to identify stiffness for the boundary impulse input experiment *AMS Contemporary Mathematics (CONM) Book Series: Proc. Conf. on Inverse Problems and Applications (Pisa, Italy)* vol 333, ed G Alessandrini and G Uhlmann (Providence, RI: American Mathematical Society)
- [10] Ji L and McLaughlin J 2003 Shear stiffness identification in biological tissues: the full elastic model *Preprint*
- [11] Keller J B 1958 A geometrical theory of diffraction: calculus of variations and its applications *Proc. Symp. on Applications of Mathematics* vol 8 (New York: McGraw-Hill) pp 27–52
- [12] Ludwig D 1966 Uniform asymptotic expansions at a caustic *Commun. Pure Appl. Math.* **19** 215–50
- [13] Maslov V P and Fedoriuk M V 1981 *Semi-Classical Approximation in Quantum Mechanics* (Dordrecht: Reidel)
- [14] Ophir J, Cespedes I, Ponnekanti H, Yazdi Y and Li X 1991 Elastography: a quantitative method for imaging the elasticity of biological tissues *Ultrason. Imag.* **13** 111–34
- [15] Ophir J, Garra B, Kallel F, Konofagou E, Krouskop T, Righetti R and Varghese T 2000 Elastographic imaging *Ultrasound Med. Biol.* **26** S23–9
- [16] Sandrin L, Tanter M, Catheline S and Fink M 2002 Shear modulus imaging with 2-D transient elastography *IEEE Trans. Ultrason. Ferroelectr. Freq. Control* **49** 426–35
- [17] Sandrin L, Tanter M, Gennisson J-L, Catheline S and Fink M 2002 Shear elasticity probe for soft tissues with 1-D transient elastography *IEEE Trans. Ultrason. Ferroelectr. Freq. Control* **49** 436–46
- [18] Schumaker L L 1981 *Spline Functions: Basic Theory* (New York: Wiley)
- [19] Taylor L S, Porter B C, Rubens D J and Parker K J 2000 Three-dimensional sonoelastography: principles and practices *Phys. Med. Biol.* **45** 1477–94
- [20] Taylor M E 1976 Grazing rays and reflection of singularities of solutions to wave equations *Commun. Pure Appl. Math.* **29** 1–38
- [21] Taylor M E 1976 Grazing rays and reflection of singularities of solutions to wave equations: part II (systems) *Commun. Pure Appl. Math.* **29** 463–81
- [22] Taylor M E 1981 *Pseudodifferential Operators* (Princeton, NJ: Princeton University Press)
- [23] Van Houten E, Miga M I, Weaver J B, Kennedy F E and Paulsen K D 2001 Three-dimensional subzone-based reconstruction algorithm for MR elastography *Magn. Reson. Med.* **45** 827–37
- [24] Walker W F and Trahey G E 1994 A fundamental limit on the performance of correlation based phase correction and flow estimation techniques *IEEE Trans. Ultrason. Ferroelectr. Freq. Control* **41** 644–54
- [25] Wu Z, Taylor L S, Rubens D J and Parker K J 2002 Shear wave focusing for three-dimensional sonoelastography *J. Acoust. Soc. Am.* **111** 439–46